Journal of Electronic Materials
https://doi.org/10.1007/s11664-026-12919-6

ORIGINAL RESEARCH ARTICLE

Dipotassium Tartrate Hemihydrate Single Crystals: XRD, Optical, Electrical Transport and SHG Investigations

E. Mohanapriya[1] · N. Sivakumar[2] · Ali Alsulmi[3] · K. Sivakumar[4] · Jan Janczak[5] · N. Kanagathara[1]

Received: 16 December 2025 / Accepted: 5 May 2026

Abstract

Single crystals of dipotassium tartrate hemihydrate (DPTH) [$K_2C_4H_4O_6 \cdot 0.5H_2O$] were grown by the slow evaporation solution technique at room temperature. According to previously reported single-crystal X-ray diffraction (SC-XRD) data, DPTH crystallizes in the monoclinic system with a non-centrosymmetric space group *I*2. The obtained crystalline DPTH was subjected to vibrational, nuclear magnetic resonance (NMR), ultraviolet–visible (UV–Vis), photoluminescence (PL), and dielectric analysis. Fourier transform infrared (FT-IR) and Fourier transform Raman (FT-Raman) spectral analysis revealed that the molecular structure contains the dipotassium cation along with L-tartrate anions. The presence of a molecular environment with hydrogen and carbon in the molecule was represented by the proton and carbon NMR spectrum. The transparency of the entire visible region was shown by the UV–Vis spectra, and 327.94 nm was determined to be the lowest cutoff wavelength. The electrical transport behavior of DPTH was investigated through frequency-dependent dielectric constant and dielectric loss studies, providing insight into the polarization mechanisms, charge displacement, and alternating-current (AC) conduction behavior within the crystal lattice. The observed low dielectric loss at higher frequencies suggests minimal energy dissipation, which is favorable for optoelectronic and nonlinear optical (NLO) device applications. The second-harmonic generation (SHG) efficiency of the DPTH crystal was about 0.66 of the standard potassium dihydrogen phosphite (KDP), indicating its potential for NLO applications. Crystal Explorer software was utilized to compute both the two-dimensional (2D) fingerprint plot and the Hirshfeld surface, offering valuable insights into the overall packing features of the produced DPTH crystal.

Keywords FT-IR · FT-Raman · optical transparency · photoluminescence · Hirshfeld

Introduction

Dipotassium L-tartrate hemihydrate (hereafter DPTH) is a dipotassium salt of tartaric acid crystallizing in a non-centrosymmetric structure with a hemihydrate network.[1] Non-centrosymmetry is a fundamental requirement for second-order nonlinear optical (NLO) activity, making DPTH a promising candidate for frequency-conversion applications. Organic materials possess easily polarizable donor–acceptor (push–pull) systems, making them highly suitable for applications in two-photon absorption, optoelectronics, optical data storage, organic light-emitting diodes (LEDs), and photovoltaic devices.[2–5] Tartaric acid is an α-hydroxyl carboxylic acid, which forms a compound suitable for second-harmonic generation (SHG) when it reacts with various salts.[6] The organic crystals contain carboxyl (COOH) and hydroxyl (OH) functional groups, capable of engaging in non-covalent interactions (NCI) that play an important role in molecular

✉ N. Kanagathara
kanagatharan.sse@saveetha.com; kanagathaara@gmail.com

1 Department of Physics, Saveetha School of Engineering, Saveetha Institute of Medical and Technical Sciences, Saveetha University, Thandalam, Chennai 602 105, India

2 Functional Materials Research Laboratory (FMRL), Department of Physics, Sri Sai Ram Engineering College, West Tambaram, Chennai 600 044, India

3 Department of Chemistry, College of Science, King Saud University, 11451 Riyadh, Saudi Arabia

4 Department of Chemistry, School of Sciences, Vels Institute of Science Technology and Advanced Studies (VISTAS), Pallavaram, Chennai 600117, India

5 Institute of Low Temperature and Structure Research, Polish Academy of Sciences, Okólna 2 str., 50-422 Wrocław, Poland

Published online: 27 May 2026

recognition. Tartrate crystals have also found applications in crystal oscillators and transducer technologies owing to their favorable dielectric and mechanical properties.[7] Previous studies have reported the optical, mechanical, and spectroscopic properties of tartaric-acid-based crystals with specific emphasis on their NLO behavior. Khan et al. investigated the mechanical stability and ultrafast spectroscopic response of L-tartaric acid crystals,[8] while Sasikala et al. theoretically predicted strong second- and third-order nonlinear responses suitable for laser frequency-doubling and optical-limiting applications.[9] Balaji et al. demonstrated enhanced optical nonlinearity, electro-optic coefficients, and ultrafast response in toluidine tartrate crystals.[10] Several organic and semi-organic tartrate crystals have been investigated including imidazolium L-tartrate,[2] ammonium tartrate,[6] toluidine tartrate,[10] L-histidinium L-tartrate hemihydrate,[11] strontium tartrate,[12] anilinium L-tartrate,[13] calcium tartrate tetrahydrate,[14] and hydroxyethylammonium-D-tartrate monohydrate.[15] Early investigations by Srivastava et al.[16] and Bhattacharjee et al.[17] reported the crystal growth and vibrational characterization of dipotassium tartrate.

Potassium ions are known to influence polarizability, dielectric behavior, and frequency-conversion efficiency in well-established NLO crystals such as potassium dihydrogen phosphate (KDP) and potassium titanyl phosphate (KTP).[18–21] However, the role of potassium in organic tartrate systems, particularly its influence on the dielectric dispersion and optical response, has not been studied. Ashfaq et al. conducted a detailed density functional theory (DFT) and single-crystal analysis of a novel pyrimethamine-based co-crystal salt, revealing valuable insights into its structural properties and stability.[22] Similarly, Tahir et al. explored the stability and molecular interactions of a 2,4-diamino-5-(4-chlorophenyl)-6-ethylpyrimidin-1-ium salt, emphasizing the importance of understanding such interactions in the design of stable organic salts.[23] Furthermore, recent work by Mashhadi et al. on 2,4-dioxothiazolidine-5-acetic acid-based organic salts highlighted their antioxidant properties and structural characteristics using both single-crystal X-ray diffraction (SC-XRD) and DFT approaches.[24] Collectively, these studies underscore the critical role of crystallographic and theoretical analyses, including intermolecular contact analysis through Hirshfeld surface studies, in advancing our understanding of organic salts and their potential applications.[22–26]

In this context, the present work aims to provide a comprehensive spectroscopic, optical, and dielectric investigation of DPTH single crystals. In addition to optical and vibrational studies, an understanding of the electrical transport behavior through dielectric analysis is crucial for evaluating the suitability of DPTH for optoelectronic and frequency-conversion applications. The SHG analysis confirms the NLO efficiency of DPTH, highlighting its potential for frequency-doubling applications. Additionally, Hirshfeld surface analysis provides a quantitative understanding of the intermolecular interactions governing crystal packing and stability. This combined experimental approach establishes DPTH as a promising semi-organic NLO material with enhanced optical and dielectric functionality.

Experimental

Dipotassium L-tartrate hemihydrate was purchased from Sigma-Aldrich (CAS number 6100-19-2). DPTH (4 g) was dissolved in distilled water (100 ml), and the resulting solution was stirred at 35°C to obtain a clear, transparent solution with a slightly alkaline reaction (pH = 8). The concentration of dipotassium L-tartrate ($K_2C_4H_4O_6$) in the initial solution left to crystallize was 0.17 mol/dm^3 (i.e., ~4% wt). The solution was then left at room temperature to crystallize. After 5 days, transparent, good-quality single crystals of $K_2C_4H_4O_6 \cdot 0.5H_2O$ were obtained (Fig. 1).

Characterization

To study the structural, optical, electronic, and NLO properties of the synthesized DPTH crystal, a range of characterization techniques were employed. The obtained single crystals were examined on an Agilent Xcalibur kappa-geometry four-circle diffractometer equipped with a Sapphire2 CCD detector. The unit cell lattice parameters are consistent with previously published SC-XRD data.[1] FT-IR spectroscopy (Bruker IFS 88) was employed to identify functional groups, while FT-Raman spectroscopy (FRA 106 accessory) was

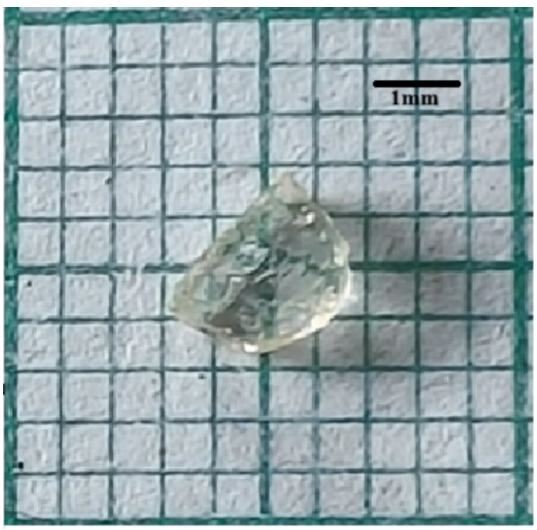

Fig. 1 Dipotassium tartrate hemihydrate (DPTH) crystal with dimensions of approximately 4.3 × 3.9 × 1.7mm^3.

performed to provide complementary vibrational information. Nuclear magnetic resonance (NMR) spectroscopy (Bruker Avance 300 MHz) was conducted for molecular-level confirmation of hydrogen environments and structural integrity. Ultraviolet–visible (UV–Vis) spectroscopy (PerkinElmer Lambda 35) was used to assess optical absorption and determine the bandgap. The grown crystal material was crushed into powder for the photoluminescence (PL) study. The PL analysis (PerkinElmer spectrofluorometer) revealed emission characteristics and electronic transitions. Hirshfeld surface analysis (Crystal Explorer 3.1) was conducted to visualize intermolecular interactions and quantify close contacts to evaluate crystal packing stability.[27] Dielectric studies (HIOKI IM3536 LCR meter) were carried out to measure the frequency-dependent dielectric constant and loss, relevant for electronic applications. Finally, SHG measurements (Ocean Optics Flame-T CCD spectrograph) confirmed the crystal's non-centrosymmetric nature and NLO activity, supporting its potential for photonic and laser technologies.

Results and Discussion

SC-XRD Analysis

The obtained single crystals were examined on a four-circle kappa-geometry Agilent Xcalibur diffractometer equipped with a Sapphire2 area CCD detector. The crystal system, space group, and lattice parameters of DPTH were in agreement with those of previously reported SC-XRD data.[1] According to the literature, DPTH crystallizes in a monoclinic system with a non-centrosymmetric space group *I*2. All the refinement SC-XRD parameters are given in Table SI.[1] The asymmetric unit and crystal packing of dipotassium *L*-tartrate hemihydrate ($K_2C_4H_4O_6 \cdot 0.5H_2O$) are shown in Figs. S1 and S2 in the supplementary materials.

Vibrational Analysis

The distinctive vibrations of the dipotassium cation and L-tartrate anion serve as the basis for the vibrational spectral analysis. The hydroxyl, carboxylate, and carbonyl groups are among the vibrations of the tartrate anion group. The carbonyl group (C=O) in tartaric acid is joined to one hydroxyl group (–OH) at the ortho position. In addition, the hydroxyl group is attached to meta positions of carbonyl groups in the other half-plane. The FT-IR and FT-Raman vibrational spectra of DPTH are shown in Figs. 2 and 3. The hydroxyl (OH), keto (C=O), and carboxyl (COOH) function groups give rise to stretching and bending vibrations. The vibrational spectra and the absorption bands of different vibrating molecules with respect to their intensity are listed in Table I. The

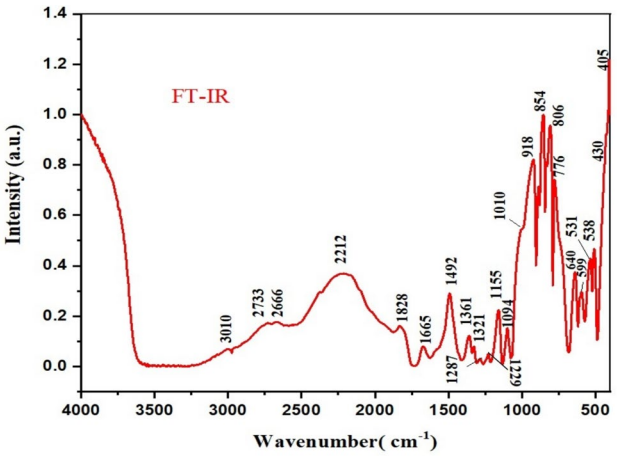

Fig. 2 Experimental FT-IR spectrum of DPTH.

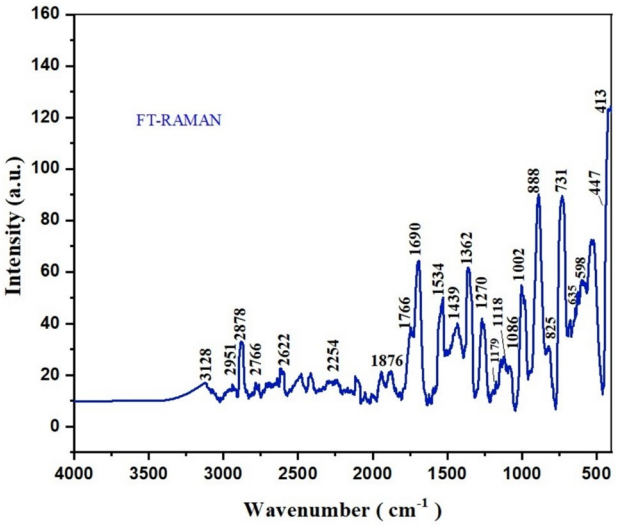

Fig. 3 Experimental FT-Raman spectrum of DPTH.

DPTH vibrational modes are observed in the range of 4000–400 cm^{-1} in both FT-IR and FT-Raman spectra. Table I provides a vibrational description for both spectra. The DPTH molecule exhibits C–C, O–H, C=O, K–O, and water molecule vibrations. Generally, the O–H stretching vibrations exhibit higher intensity and are observed in the region of 3500–3200 cm^{-1}.[28] In the DPTH compound, O–H stretching vibrations are observed at the lower frequency of 3128 cm^{-1} in the Raman spectrum, with additional weak peaks at 3010 and 2951 cm^{-1} in both the FT-IR and FT-Raman spectra. In the FT-Raman spectrum, a medium-strong stretching vibrational peak appears at 2878 cm^{-1}. These peaks confirm the presence of a hydroxyl group in the tartaric acid in the DPTH molecule. The absorption bands arising from the O–H

Table I Vibrational assignment for DPTH

FT-IR	FT-Raman	Vibration modes
–	3128 w	ν (OH)
3010 w	2951 w	ν (OH)
–	2878 ms	ν (OH), ν (CH)
2733 w	2766 w	ν (CH), ν (C=O)
2666 w	2622 w	ν (CH), ν (C=O)
2212	2254 w	ν (C=O)
1828 w	1876 w	ν (C=O), ν (OH), β (H–O–H)
–	1766 ms	ν (C=O), β (H–O–H)
1665 w	1690 s	ν (C=O), β (H–O–H)
	1633	ν (C=O), β (H–O–H)
–	1534 s	ν (C=O)
1492 w	1439 w	β (OH)
1361 w	1362 w	β (OH)
1321 w		ν (C–O)
1287 vw	1270vw	ν (CH), β (C–O–H), ν (OH)
1155 s	1179w	(C–O), ω (C–C–O)
1094 ms	1086w	ω (C–O), ω (C–C–O)
1010 w	1002 ms	ω (C–O),ν (C–C)
854 s	888 s	(K–O)
806 s	825 s	ν (C–C), (C–O), ω (C–C–O)
776 ms	731 s	ω (C–C–O), ν (OH)
640 ms	635 w	ω (O–C=O), ω (C–C–O), ω (OH)
599 w	598 w	ω (C–C–O)
538 m		(K–O)
531 m	524 w	(K–O)
430 ms	447 ms	ν (CO),ν (CC), ω (O–C=O)
405 w	413 w	ω (O–C=O)

Intensity description: *w* weak; *vw* very weak; *s* strong; *ms* medium strong

Vibrational mode description: ν stretching; β bending; ρ rocking; τ twisting; ω wagging

in-plane bending modes are observed in the region of 1440–1260 cm^{-1}.[29] O–H out-of-plane bending modes are observed in the region of 710–517 cm^{-1}.[30] In the FT-IR spectrum, these vibrations appear as faint peaks at 776 cm^{-1}, 640 cm^{-1}, and 599 cm^{-1}. In the FT-Raman spectrum, the O–H out-of-plane bending modes are present at 731, 635, and 598 cm^{-1}. In general, C–H stretching vibrations appear in the region of 3100–2900 cm^{-1}.[31] In the DPTH compound, C–H stretching vibrations are observed at 2878 cm^{-1} (medium strong) in the FT-Raman spectrum. Weak C–H stretching vibrations are observed at 2666 cm^{-1} and 2622 cm^{-1} in the FT-IR and FT-Raman spectra, respectively. C=O stretching vibrations occur in the range of 1700–1400 cm^{-1}.[32–34] In this compound, FT-IR spectrum peaks are observed at 2733, 2666, 2212, 1828, and 1665 cm^{-1}. In the FT-Raman spectrum, peaks are obtained at 2766, 2622, 2254, 1876, 1766, 1690, and 1534 cm^{-1}. In the DPTH compound, C–O stretching vibrations are observed at 1492, 1361, and 1321 cm^{-1} in the FT-IR spectrum, and at 1439 and 1362 cm^{-1} in the FT-Raman spectrum.[35] The absorption at 1534 cm^{-1} is due to the carbonyl C=O group.[35] K–O (potassium–oxygen) vibrations typically appear in the low-frequency region in the FT-IR spectrum, often below 700 cm^{-1}. Specifically, K–O stretching vibrations in potassium feldspar are observed around 531–536 cm^{-1}, 463–466 cm^{-1}, and 445 cm^{-1}.[36] In the present DPTH compound, the K–O vibrations exhibit a strong-intensity peak at 854 cm^{-1} in the FT-IR spectrum and 888 cm^{-1} in the FT-Raman spectrum. Other peaks located at 538 and 531 cm^{-1} in the FT-IR spectrum and 524 cm^{-1} in the FT-Raman spectrum are assigned to K–O bending vibrations.

Nuclear Magnetic Resonance Analysis

The ^{1}H and ^{13}C NMR spectra of the DPTH crystals are shown in Figs. 4 and 5, respectively. As the reference standard for the proton NMR data, the solvent peak (dimethyl sulfoxide = 2.50 ppm) is presented. The carbon NMR value is reported from 39.5 ppm to 40.5 ppm in DMSO solvent phase. The proton (^{1}H) NMR spectrum reveals distinctive peaks for DMSO, which appear as a septet. The peaks in the spectrum are assigned as follows: peaks at 5.06 ppm and 4.31 ppm, a peak at 3.30 ppm, and peaks in the range of 2.52 ppm to 2.49 ppm are associated with the protons connected within the molecular structure of the DPTH crystal.

In carbon NMR, the pure L-tartrate exhibits a signal at 175 ppm, while the measured compound shows a signal at 173.54 ppm. This downfield shift is attributed to electrostatic interaction and partial coordination between potassium ions and the carboxylate oxygen atoms of the tartrate anion, which alters the local electronic environment of the carbonyl carbon. The multiple closely spaced signals observed in the carbon NMR spectrum at 40.52 ppm, 40.35 ppm, 40.18 ppm, 40.01 ppm, 39.85 ppm, 39.68 ppm, and 39.51 ppm originate from the DMSO solvent used during the NMR measurements. DMSO generally produces a multiplet in this region due to magnetic non-equivalence, temperature effects, and instrumental resolution; therefore, these peaks are not assigned to chemically distinct carbon environments of the DPTH crystal. The intrinsic carbon environments of DPTH are instead confirmed by tartrate-related resonances, particularly the shifted carboxyl carbon signal at 173.54 ppm, which reflects potassium–tartrate interactions within the crystal lattice.

Tartaric acid in its pure form exhibits a signal at 73 ppm,[37] while in the present DPTH crystal a corresponding signal is observed at 72.61 ppm, further confirms the incorporation of the tartrate moiety in the dipotassium salt.

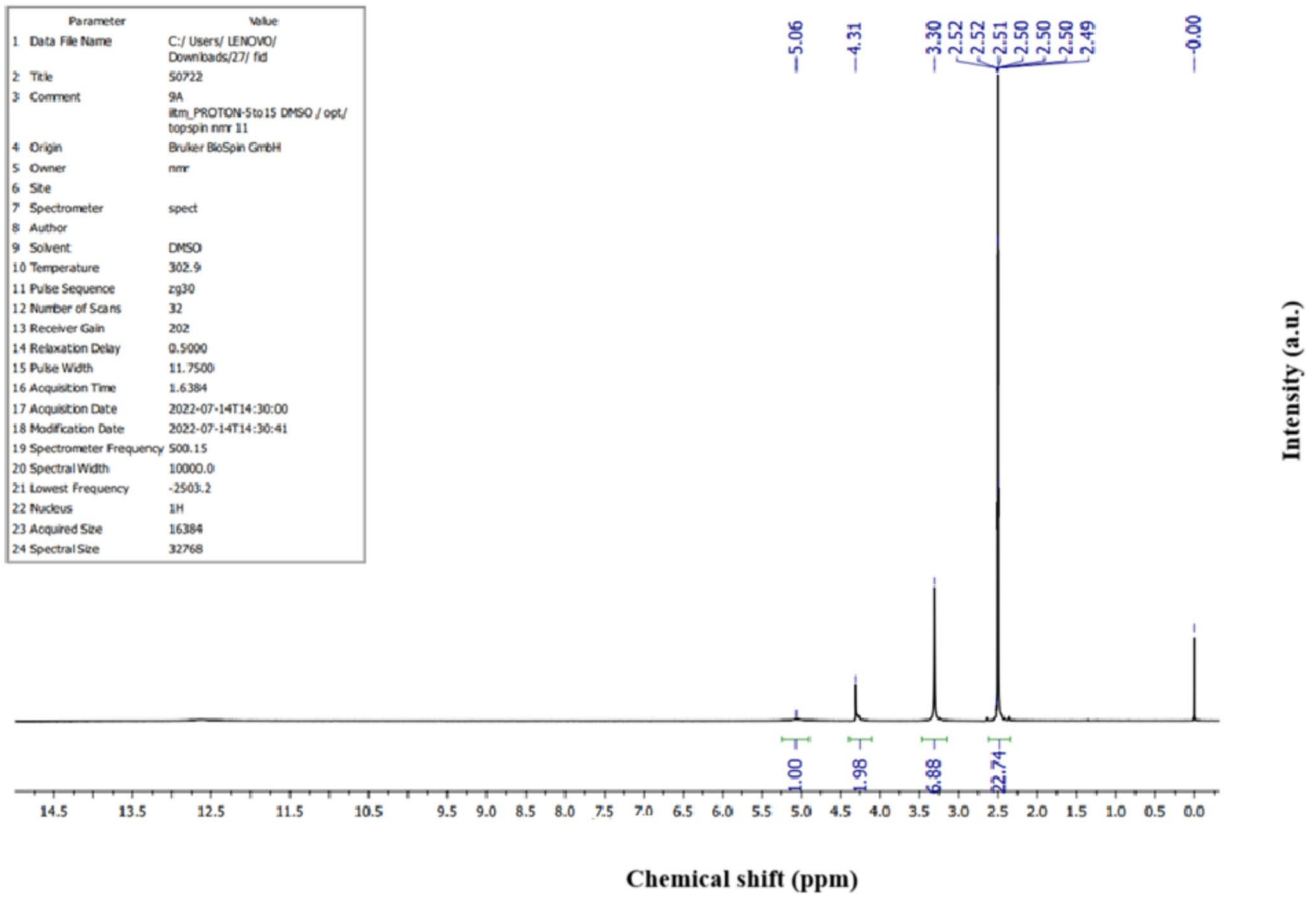

Fig. 4 Proton nuclear magnetic resonance (^{1}H NMR) spectrum of DPTH illustrating the hydrogen environment of the compound.

Overall, the combined proton and carbon NMR analysis confirms the DPTH chemical integrity of the DPTH crystal and substantiates the interaction between potassium ions and tartrate anions.

Ultraviolet–Visible Analysis

Ultraviolet–visible analysis offers significant insights into the transition range, transparency, and bandgap energy, all of which play a vital role in optical applications. Figure 6 illustrates the UV–Vis spectrum of the DPTH compound. Its absorption spectrum typically falls within the UV and visible range, which is approximately 200 nm to 800 nm. The determination of a molecule's optical bandgap involves examining electron transitions within the σ and π orbitals, where molecules shift from their ground state to higher energy levels upon absorbing UV and visible light. The crystal's impressive optical clarity and its lower cutoff wavelength render it a highly effective choice for NLO devices, laser frequency doubling, and optoelectronic applications.[38] The UV–Vis spectrum of DPTH reveals a prominent absorption peak at 296.07 nm, signifying the compound's highest light absorption intensity at this wavelength. This peak is probably linked to an n–π^* transition, where an electron undergoes excitation from a filled n^{th} orbital to an empty π^* (antibonding) orbital.[39,40] The occurrence of conjugated systems or aliphatic structures within the DPTH molecule is expected to contribute to these transitions. The lower cutoff wavelength is found to be 327.94 nm, and after that, the transparency in the entire visible region is found to be sufficient for use of the material in optical applications. Further, Tauc plots were drawn to identify the energy gap of the material, which is depicted in Fig. 6 [inset] by taking energy ($h\upsilon$) and $(\alpha h\upsilon)^2$ along the X- and Y-axis, respectively. By extending the linear segment of the graph to the X-axis, specifically where $(\alpha h\upsilon)^2$ equals zero, the optical bandgap energy of the crystal which is calculated as 4.288 eV, and it can be considered a suitable candidate for wide-bandgap semiconductor and optical device applications.

Photoluminescence Studies

Photoluminescence (PL) occurs when the excited state that emits light is created through the absorption of photons.[41]

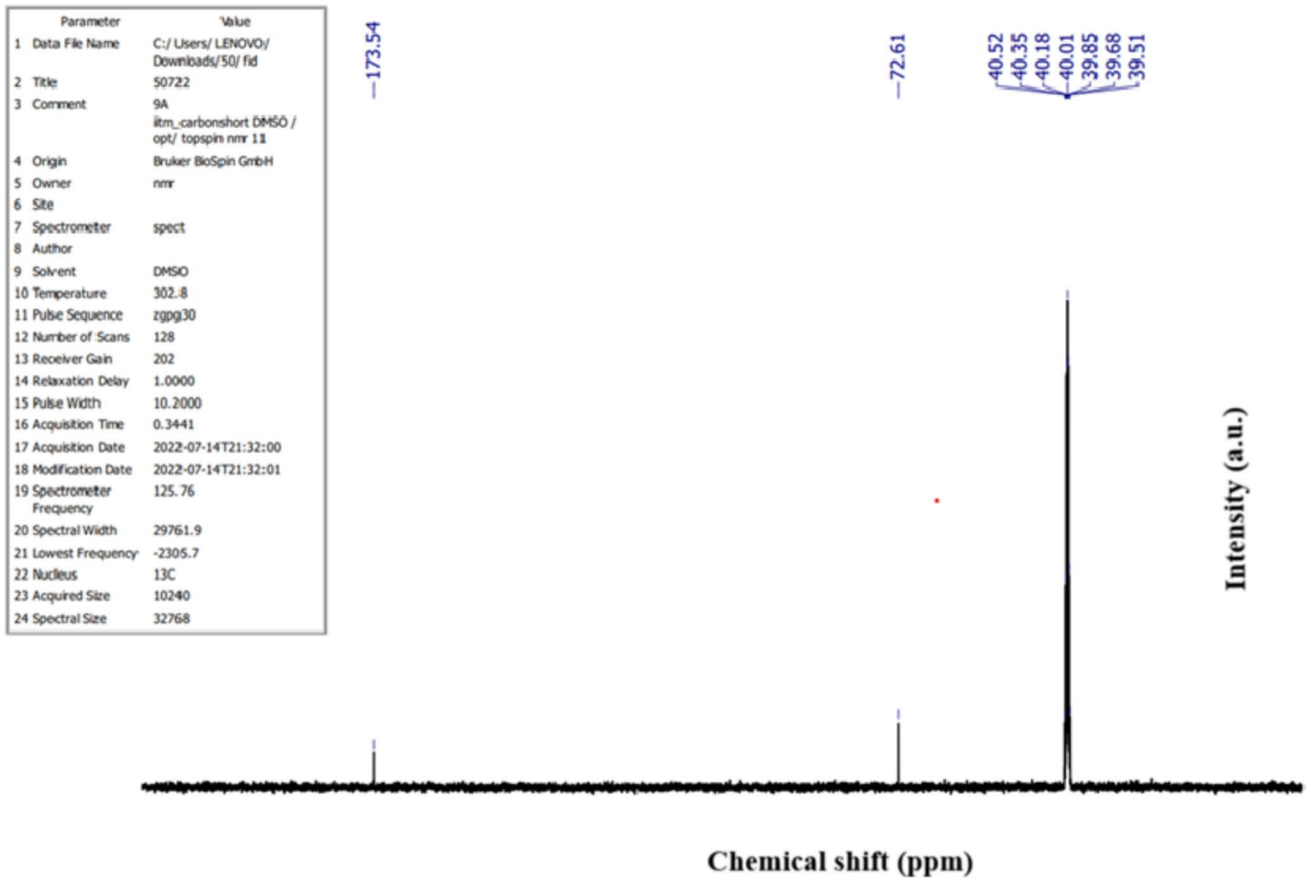

Fig. 5 ^{13}C NMR spectrum of DPTH depicting the distribution of carbon environments within the compound.

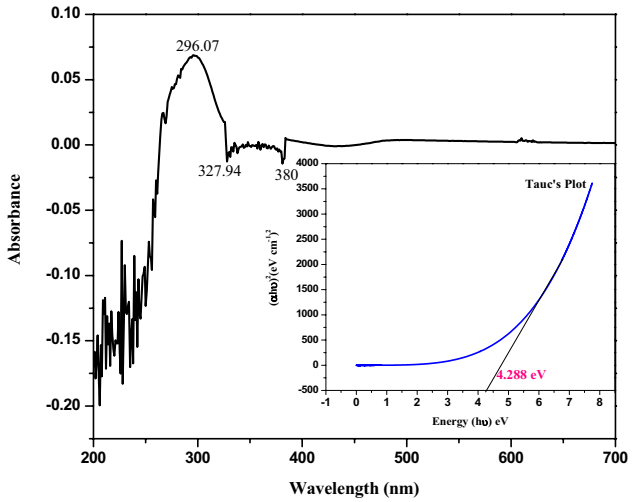

Fig. 6 UV–visible absorption spectrum and Tauc plot (inset) of DPTH.

The process of excitation can take the form of either a single photon or a multiple photons. PL spectroscopy serves as a powerful technique for examining molecular-level energy levels, physical properties of materials, and energy gap states, as well as shallow and deep-level defects. A distinct peak becomes evident at 389 nm, implying that the electronic transition likely entails the transfer of electrons from an anti-bonding orbital to a bonding orbital (π^*–π). The emission wavelength at this value suggests that DPTH could be advantageous for applications involving violet-colored LED emissions. However, the wide emission peak centered at 389 nm indicates violet light emission and is indicative of the charge transfer process, along with the trapping of electrons. This phenomenon is attributed to the involvement of shallow holes transitioning to deeper hole states.[42,43] In Fig. 7, a significant intense emission peak at 389 nm (with an energy gap of 3.18 eV) corresponds to excitons near the band edge within the DPTH crystal. The energy estimated from PL (3.18 eV) is less than the bandgap energy (4.28 eV), suggesting the presence of sub-bandgaps called traps between the valance band and conduction bands. The recombination of electrons and holes at the sub-bandgaps is mostly non-radiative, such as Shockley–Read–Hall (SRH) recombination. This energy loss is dissipated as heat and not light.[44] Thus, the radiative recombination often requires the assistance of phonons, leading to low-energy peaks in PL

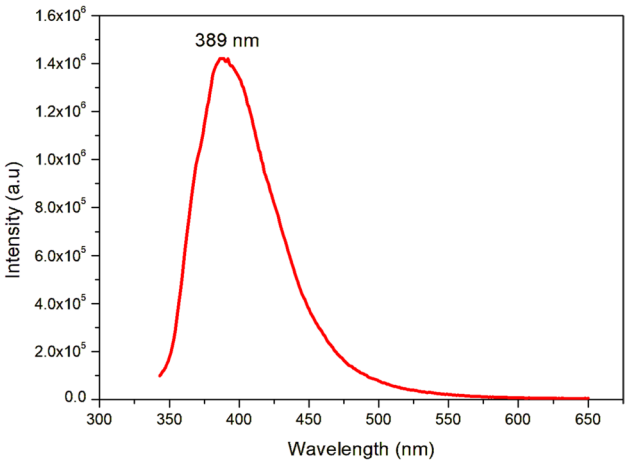

Fig. 7 Photoluminescence spectrum of DPTH.

emission. The presence of O–H, N–H–O, and O–H–I bonds in the prepared materials could lead to the development of defect states, which are also responsible for the low energy.[45] Thus, the PL analysis provides insights into the optical and electronic characteristics of the DPTH crystal, confirming its potential applicability in optoelectronic devices, particularly violet LEDs.[46,47]

Hirshfeld Surface Analysis

A three-dimensional (3D) molecular surface Hirshfeld analysis was performed, accompanied by the generation of a two-dimensional (2D) fingerprint for the compound. This analysis assists in understanding the molecular factors influencing crystal packing, underscoring the significance of identifying strong hydrogen bonds and other weak non-covalent interactions for crystal formation.[48–50] Hirshfeld surface analysis was carried out using Crystal Explorer software 3.1. Figure 8a illustrates the Hirshfeld surfaces of DPTH with mapped d_{norm}, d_i, and d_e. Figure 8b depicts the various interactions of K–O (41.9%), O–H (31.6%), K–H (10.2%), H–H (9.5%), O–O (3.5%), C–H (2.2%), C–K (0.7%), and C–O (0.4%) present in the DPTH crystal. The primary contribution to strong hydrogen bond interactions, comprising 41.9%, arises from potassium–oxygen interactions. Additionally, the Hirshfeld surface analysis reveals that oxygen-hydrogen interactions constitute 31.6%, potassium-to-hydrogen interactions make up 10.2%, and hydrogen itself occupies 9.5% of the DPTH molecule. The remaining intermolecular contacts consist of O–O interactions at 3.5%, C–H at 2.2%, C–K at 0.7%, and C–O at 0.4%. Interactions between atoms, specifically K–O, O–H, and K–H bonds, are pivotal in shaping the crystal structure of the DPTH compound. These interactions contribute significantly to the arrangement of atoms, forming 3D networks. Figure 8c illustrates Hirshfeld surfaces of DPTH with mapped d_i, d_e, d_{norm}, shape index, curvedness, and fragment patch. In the map of the shape index and curvature, the red and blue regions highlight hydrogen bonding and stacking and provide similar information about the crystal's structural features. Each type of Hirshfeld surface plot provides unique insights into the molecular structure and its interactions within a crystal. The surface smoothness is established by a low curvedness value. By analyzing these surfaces together, researchers can gain a comprehensive understanding of the molecular packing, interaction strengths, and specific contact regions within the crystal lattice.

In Hirshfeld surface analysis, the process of void calculation involves quantifying and describing the unoccupied areas or voids within the structure of a crystal lattice. This analytical method offers valuable insights into the structural attributes, packing efficiency, and interactions between molecules present within crystalline materials. To evaluate the mechanical resilience of the crystal, a void analysis was conducted by aggregating the electron densities of atoms with spherically symmetric characteristics found within the asymmetric unit.[51,52] The void surface is defined as an isosurface derived from the procrystalline electron density and is computed for the entirety of the unit cell. The intersection of the void surface with the unit cell boundary and the creation of capping faces generate an enclosed volume for analysis. The volume of the crystal voids and the percentage of unoccupied space within the unit cell were determined to be 180.41 $Å^3$ and 23.3%, respectively. By comparing the calculated contacts with those that were calculated assuming that every type of contact had the same probability of forming, the enrichment ratio may be found. Based on chemical composition and aromaticity, the enrichments and contact tendencies were examined in a number of compound families.[53] The enrichment ratio for the K–O interaction in the crystal was calculated as 1.04, indicating a slight enrichment compared to what would be expected in a random distribution. The O–H interaction enrichment ratio was 0.98, suggesting it occurs almost as frequently as would be anticipated randomly. The K–H interaction showed a significantly lower enrichment ratio of 0.485, indicating a notable depletion relative to a random distribution. Similarly, the H–H interaction enrichment ratio of 0.545 showed depletion compared to random expectation.

Dielectric Studies

Dielectric studies provide detailed information on the electrical transport behavior of DPTH materials, as they are directly associated with charge displacement, polarization mechanisms, and alternating-current (AC) conduction processes. In non-centrosymmetric organic crystals, the frequency-dependent dielectric response offers insight

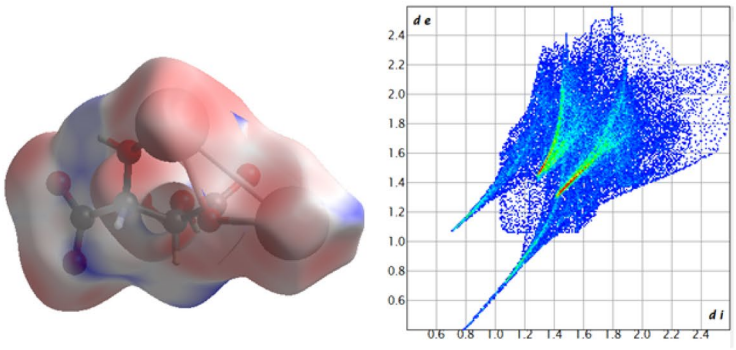

(a)

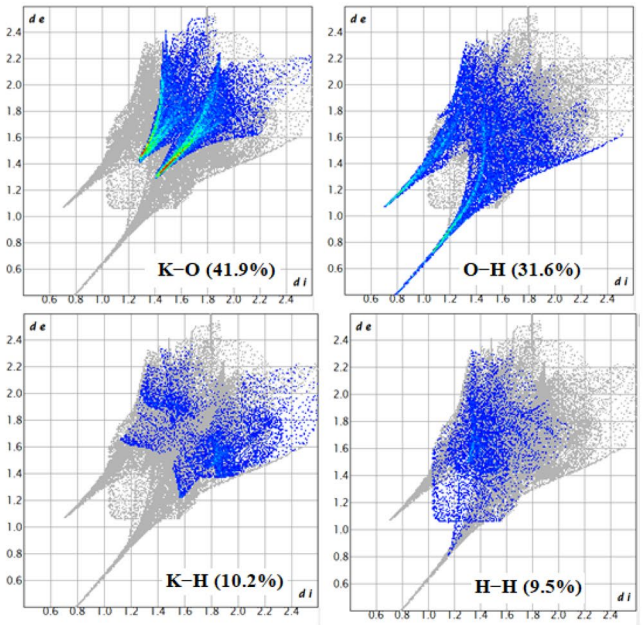

(b)

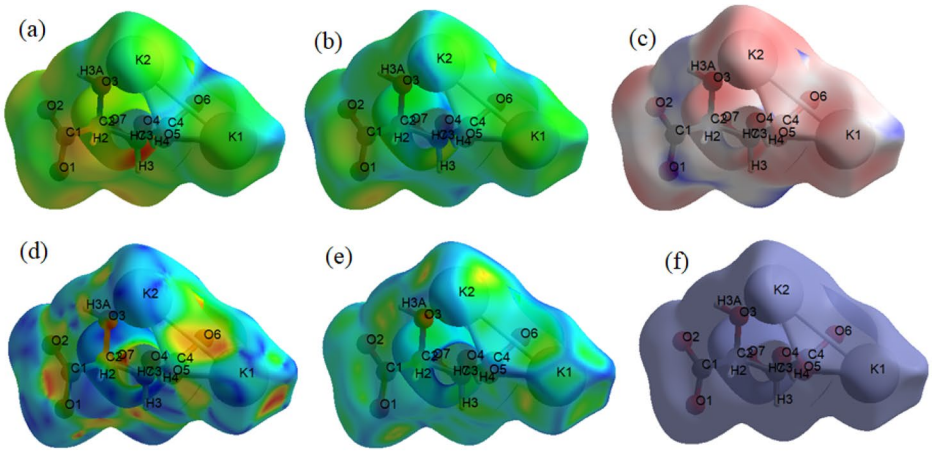

(c)

Fig. 8 (a) Complete fingerprint (100%) Hirshfeld surface for DPTH. (b) Relative contributions to the percentage of Hirshfeld surface area for the various intermolecular contacts. (c) Hirshfeld surface of DPTH plotted over (a) d_i, (b) d_e, (c) d_{norm}, (d) shape index, (e) curvedness, and (f) fragment patch.

into the mobility of charge carriers and dipolar orientation under an applied electric field. Therefore, the dielectric constant and dielectric loss measurements of DPTH were analyzed to understand its electrical transport characteristics. Dielectric analysis reveals the insulating properties of various common materials. In this study, the focus is on exploring the dielectric characteristics of the developed DPTH crystal. A notable characteristic of dielectric materials is the decrease in the dielectric constant with frequency.[54] Understanding the electro-optic features of these crystalline solids is critical, as the dielectric properties offer insights into the electric fields within the solid. The presence of several types of polarization in these materials—including dipole, ionic and electronic polarization, and space charge—is responsible for the change in permittivity in the low- to high-frequency region. The frequency dependence of electrical properties provides a clear view of material applicability in devices.[55] The dielectric constant and dielectric loss of the crystal were calculated using Eqs. (1) and (2).

$$\text{Dielectric loss, } \xi'' = \xi' \tan \delta, \tag{1}$$

$$\text{Dielectric constant } \xi' = {}^{Ct}/_{A\epsilon_0} \tag{2}$$

where C is capacitance (F), δ is loss, t is thickness (m), and A is the area of the cross-section.

The direction of polarization within the sample is opposite to the applied or external electric field, which is used to explain the electric dipole orientations.[56] In the presence of an external electric field, these dipoles undergo rotation, generating a dipole moment oriented perpendicular to the applied field direction. This phenomenon is referred to as the rotation of the polarization direction.[57,58] Figure 9a shows the variation in the dielectric constant (ε') with the logarithm of frequency (log f) in Hz, measured across a temperature range from 308 K to 378 K. At lower frequencies (log $f \approx$ 2.3–3), the dielectric constant is higher and shows significant dispersion. This behavior is most pronounced at 348 K, where ε' reaches a peak of approximately 75. As the frequency increases (log $f > 3$), the dielectric constant decreases and stabilizes, indicating a frequency-dependent dielectric relaxation, i.e., attributed to the inhibition of the ionic dipole movement.[59] At higher frequencies (log $f \approx$ 5–7), ε' values converge to a relatively constant range (~24–28), regardless of temperature. The decrease in dielectric constant with increasing frequency is attributed to the reduced contribution of space charge, dipolar, and ionic polarizations at higher frequencies. At the higher frequencies, molecular dipoles cannot deal with the varying applied electric field, and thus dielectric permittivity decreases and reaches a constant value.[60,61] A high dielectric value at low frequencies reflects the space charge polarization due to the grain

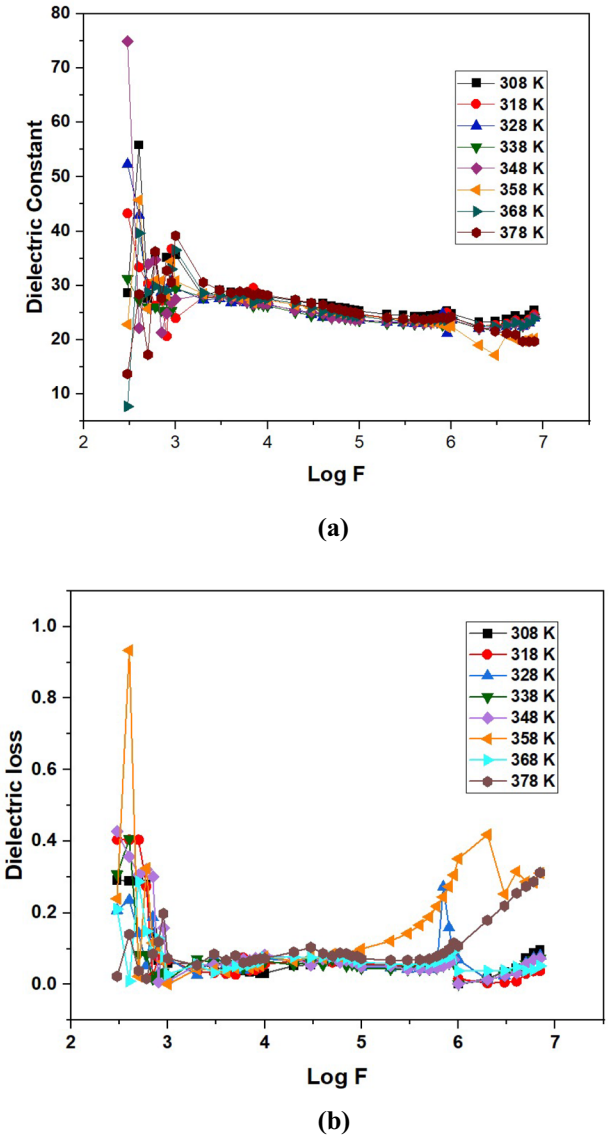

Fig. 9 (a) Dielectric constant of DPTH. (b) Dielectric loss of DPTH.

boundaries in the crystal materials. At very high frequencies, the contributions from different polarizations start decreasing and the system is unable to adopt any rapid changes in the applied electric field.[62] This behavior indicates limited long-range charge transport and dominant localized charge displacement mechanisms, which are characteristic of insulating and semi-organic NLO crystals.

Figure 9b displays the variation in dielectric loss with log f (Hz) at different temperatures ranging from 308 K to 378 K. At lower frequencies (log $f \approx$ 2.3–3), the dielectric loss is relatively high, with noticeable peaks—especially at 358 K, where a sharp peak reaching ~1.0 is observed. This behavior is attributed to interfacial (Maxwell–Wagner) polarization and space charge effects, which dominate

at low frequencies. As the frequency increases ($\log f > 3$), the dielectric loss drops significantly and remains low and stable in the mid-frequency region ($\log f \approx 4$–5). However, a secondary rise in dielectric loss appears at higher frequencies, particularly at elevated temperatures of 358 K and 378 K, possibly due to dipolar relaxation or conduction losses.[62–65] The active (ohmic) component of the current increases more rapidly than its reactive (capacitive) component, and hence dielectric loss increases. However, at higher frequencies ($\log f \approx 5$–6), dielectric loss decreases with increasing frequency, as the reactive component increases in proportion to the frequency, whereas the active component of the current is practically independent of frequency.[66] The maxima of dielectric loss shift towards higher frequencies ($\log f \approx 6$–7), and the heights of the peaks also increase with increasing temperature. This trend in dielectric material is due to the increase in the number of charge carriers for conduction, which is realized as a decrease in the resistivity of the sample.[67] The shifting of relaxation peak position in the high-frequency region indicates that the charge carriers are thermally activated.[65] A peak broadening which is slightly asymmetrical in nature can be observed with a rise in temperature. The broadening of the peak indicates the presence of temperature-dependent electrical relaxation.[68] The low dielectric loss observed at higher frequencies suggests minimal energy dissipation and suppressed charge carrier hopping within the crystal lattice. Such electrical transport behavior is advantageous for optoelectronic and NLO applications, as it ensures stable polarization response under high-frequency electric fields. Furthermore, the dielectric properties are influenced by factors such as temperature, frequency, and presence of impurities. Notably, the lower dielectric constant and dielectric loss at higher frequencies suggest a limited presence of electrically active defects in the produced crystal, making it suitable for NLO applications.

Electrical Conductivity Studies

Figure 10 illustrates the electrical conductivity (σ_{ac}) of the DPTH single crystal over a temperature range of 308–378 K with a step value of 10 K for different frequencies. The dependence of σ_{ac} on frequency for the DPTH crystal can be expressed by the following relation.

$$\text{Electrical resistivity } (\rho) = \frac{A}{2\pi f C d} \tag{3}$$

$$\text{Electrical conductivity } (\sigma) = \frac{1}{\rho}, \tag{4}$$

where C is capacitance (F), d is thickness (m), and f is frequency (Hz).

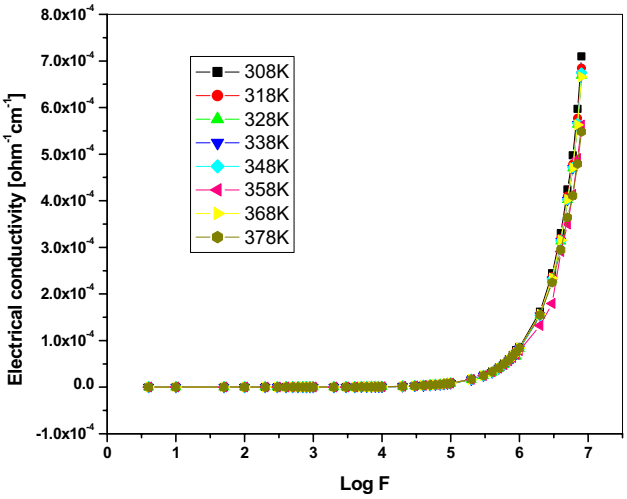

Fig. 10 Electrical conductivity of the DPTH.

The AC conductivity curve can be explained in two regions—a flat or plateau region at low angular frequency and a dispersion region at high frequency. The frequency that separates the dispersion region from the plateau region is referred to as the characteristic frequency (ω_p), which is also known as the hopping rate.[69] As can be seen in Fig. 10, σ_{ac} increases as frequency increases due to the rapid vibration of ions when compared to the low-frequency region. The alternating electric field changes direction too slowly at low frequencies, making it difficult for charge carriers (such as ions or localized electrons) to react to it. Thus, the trapping effect or interfacial polarization limits their mobility. The carriers are better able to follow the faster alternating field as the frequency rises. Hopping conduction, such as ion hopping or dipolar relaxation, can take over as a result of the reduced impact of polarization.[70] At lower frequencies, electrical conductivity is found to be independent of frequency and is referred to as the direct-current (DC) conductivity (σ_{dc}) of the material. The conductivity in this region is attributed to ionic charge carriers which undergo a random diffusion process through activated hopping. The high-frequency region shows increased conductivity, attributed to the enhanced mobility of charge carriers, as described by Jonscher's power law.[71] The increasing trend of conductivity with frequency indicates hopping conduction of protons through hydrogen bonds.[72] As the frequency increases, the conduction hopping will decrease with the limited interatomic distances and will no longer be randomly distributed.[73]

Second-Harmonic Generation Studies

The SHG efficiency of the DPTH crystal in comparison with the well-established potassium dihydrogen phosphate (KDP)

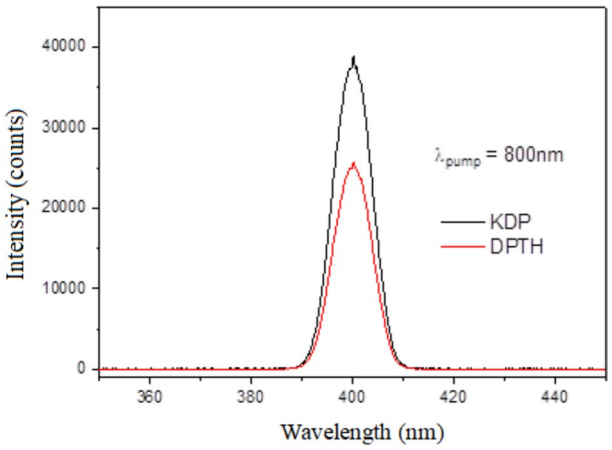

Fig. 11 SHG response of KDP and DPTH.

was investigated using the Kurtz–Perry method.[74,75] The experiment used ultrasmall microcrystals, between 177 µm and 250 µm in size, carefully placed on glass slides for stability. An 800-nm laser was chosen because it works well with both DPTH and KDP. The laser was set up precisely and operated at 293 K to conduct the Kurtz–Perry test. To detect the SHG signal from crystal samples, we used backscattering geometry at a 45° angle for precise capture. This setup minimized interference from other light sources. Additionally, a specialized short-pass filter was used to enhance signal clarity by removing any unwanted radiation, isolating the SHG response of the crystals. The data were collected using an advanced CCD spectrograph to accurately record and analyze spectral information. Each compound was measured 30 times to reduce experimental variation. The measurements were averaged over 75 ms to ensure reliability and precision. After the experimental steps, both DPTH and KDP crystals were closely examined for their ability to generate second-harmonic signals. Figure 11 depicts the comparative SHG signal intensity of DPTH and KDP. The SHG efficiency of DPTH is about 0.66 of the standard KDP efficiency, indicating its potential in NLO applications. The observed SHG response of DPTH reveals its unique optical characteristics and potential for use in optical devices and photonics, indicating the need for more research in this area.

Conclusion

DPTH crystals were grown via the slow evaporation method at room temperature. A thorough vibrational spectrum analysis, considering peak positions and relative intensities, allowed for the assignment of fundamental bands in DPTH. Additionally, the structure of the DPTH crystal was validated through proton and carbon NMR spectroscopy investigations. The wide optical transparency and a direct optical bandgap of 4.288 eV, together with a strong absorption edge at 296.07 nm, clearly establish DPTH as a promising UV-filtering material, suitable for blocking harmful UV radiation while maintaining visible transparency. The observed PL emission at 389 nm, combined with good dielectric behavior at lower frequencies, indicates that DPTH can be considered for optoelectronic integrated devices, such as UV photodetectors, light-emitting components, dielectric layers, and insulating materials in microelectronic and photonic circuits. These properties support its potential integration into multifunctional optoelectronic fields. The dielectric nature of DPTH, characterized by increased dielectric constant and loss at lower frequencies, suggests its potential application in capacitors and insulating materials and in the development of dielectric resonators for microwave devices. Hirshfeld surfaces and 2D fingerprint plots were generated to visually represent intermolecular interactions in the crystal structure, serving as graphical tools for comprehending crystal packing. The associated two-dimensional fingerprint map highlights the major and targeted interactions, particularly between dipotassium and oxygen, constituting more than 41.9% of the Hirshfeld surface. Moreover, the non-centrosymmetric crystal structure and measurable SHG efficiency (0.66 times that of KDP), along with optical transparency in the visible region, highlight the suitability of DPTH for NLO frequency conversion applications. Although the SHG efficiency is moderate, the intrinsic nonlinear response, structural stability, and ease of crystal growth make DPTH a viable candidate for frequency-doubling and photonic modulation devices. Overall, the combined optical, dielectric, photoluminescence, and nonlinear properties position DPTH as a multifunctional material with suitable prospects in UV filtering, optoelectronic integration, and NLO applications, warranting further optimization and device-level investigations.

Supplementary Information The online version contains supplementary material available at https://doi.org/10.1007/s11664-026-12919-6.

Acknowledgments Dr. N. Sivakumar and Dr. Ali Alsulmi acknowledge the financial support through the Researchers Supporting Project scheme (RSP-2025-78), King Saud University, Riyadh, Saudi Arabia.

Author Contributions E. Mohanapriya: Writing–original draft, Conceptualization, Methodology. N. Sivakumar: Writing–review and editing, Resources. Ali Alsulmi: Resources. K. Sivakumar: Investigation. Jan Janczak: Writing–review & editing, Visualization, Validation. N. Kanagathara: Writing–original draft, Investigation, Validation.

Data Availability All data supporting this study will be provided based on request.

References

1. R. Boese, D. Bläser, R. Latz, and M. Piennisch, Dipotassium tartrate hemihydrate. *Acta Crystallogr. C Struct. Chem.* 51, 2227–2229 (1995).

2. H. Raval, B.B. Parekh, K.D. Parikh, and M.J. Joshi, Growth and characterizations of organic NLO imidazolium L-tartrate (IMLT) single crystal. *Adv. Condens. Matter. Phys.* 2019, 1–9 (2019).
3. S.R. Forrest, and M.E. Thompson, Introduction: organic electronics and optoelectronics. *Chem. Rev.* 107, 923–925 (2007).
4. G.S. He, L.S. Tan, Q. Zheng, and P.N. Prasad, Multiphoton absorbing materials: molecular designs, characterizations, and applications. *Chem. Rev.* 108, 1245–1330 (2008).
5. Y. Ohmori, Development of organic light-emitting diodes for electro-optical integrated devices. *Laser Photon. Rev.* 4, 300–310 (2009).
6. N. Kalaimani, K. Ramya, R. Aarthi, and C.R. Raja, Growth and characterization of solution grown nonlinear optical ammonium tartrate crystal. *J. Chem.* 11, 1263–1269 (2018).
7. P.E. Teresa, M. Sornambol, S. Gowri, J. Aarthi, and M. Navina, Growth, spectral, dielectric, magnetic and antimicrobial studies on dye doped Rochelle salt crystal. *Results Mater.* 6, 100095 (2020).
8. N. Khan, N. Vijayan, K. Shandilya, R. Kumar, A. Krishna, S. Chopra, and M. Jewariya, Single crystal growth of L-tartaric acid and its characterization for optical applications. *J. Mater. Sci. Mater. Electron.* 31, 4494–4502 (2020).
9. V. Sasikala, D. Sajan, N. Vijayan, K. Chaitanya, M.S. Babu Raj, and B.H. Selin Joy, Growth, molecular structure, NBO analysis and vibrational spectral analysis of L-tartaric acid single crystal. *Spectrochim. Acta A Mol. Biomol. Spectrosc.* 123, 127–134 (2014).
10. J. Balaji, P. Srinivasan, S. Prabu, M. George, and D. Sajan, Growth and dielectric studies of toluidine tartrate single crystals: a novel organic NLO material. *J. Mol. Struct.* 1207, 127750 (2020).
11. N. Kanagathara, V.J. Thanigaiarasu, V. Ragavendran, M.K. Marchewka, L. Saravanan, and A.Y. Lo, Quantum computational investigation into structural, spectroscopic, topological and electronic properties of L-histidinium-L-tartrate hemihydrate: nonlinear optical organic single crystal. *Heliyon* 9(4), e14879 (2023).
12. S.K. Arora, V. Patel, B. Amin, and A. Kothari, Dielectric behaviour of strontium tartrate single crystals. *Bull. Mater. Sci.* 27, 141–147 (2004).
13. N. Kanagathara, M.K. Marchewka, G. Anbalagan, A. Ben Ahmed, and H. Feki, Molecular structure, vibrational spectra and first order hyperpolarizability of anilinium L-tartrate monohydrate (ALTM). *J. Optoelectron. Adv. Mater.* 19, 251–265 (2017).
14. X.S. Shajan, and C. Mahadevan, On the growth of calcium tartrate tetrahydrate single crystals. *Bull. Mater. Sci.* 27, 327–331 (2004).
15. Y. Zhang, Y. Wang, Y. Che, and J. Zheng, Growth and properties of two new organic nonlinear optical crystals: hydroxyethylammonium-L-tartrate monohydrate and hydroxyethylammonium-D-tartrate monohydrate. *J. Cryst. Growth* 299, 120–124 (2007).
16. G.P. Srivastava, S. Mohan, and Y.S. Jain, Laser Raman and infrared spectra of di-potassium tartrate hemihydrate. *J. Raman Spectrosc.* 13, 25–29 (1982).
17. R. Bhattacharjee, Y.S. Jain, and H.D. Bist, Laser Raman and infrared spectra of dipotassium tartrate hemihydrate. *J. Raman Spectrosc.* 20, 561–567 (1989).
18. Y. Zhu, M. Li, H. Yin, P. Wang, J. Huang, and H. Liu, Growth and characterization of KDP crystals grown by the 2D-translation method equipped with continuous filtration. *Cryst. Growth Des.* 20(6), 3772–3779 (2020).
19. N. Zaitseva, and L. Carman, Rapid growth of KDP-type crystals. *Prog. Cryst. Growth Charact. Mater.* 43, 1–118 (2001).
20. M. Qin, X. Xu, G. Yu, B. Wang, and W. Cheng, Rapid growth of KDP crystals in the direction. *Crystals* 10, 108 (2020).
21. S. Neufeld, A. Bocchini, U. Gerstmann, A. Schindlmayr, and W.G. Schmidt, Potassium titanyl phosphate (KTP) quasiparticle energies and optical response. *J. Phys. Mater.* 2(4), 045003 (2019).
22. M. Ashfaq, G. Bogdanov, V. Glebov, A. Ali, M.N. Tahir, and S. Abdullah, Single crystal investigation, Hirshfeld surface analysis and DFT exploration of the pyrimethamine-based novel organic salt: 2,4-diamino-5-(4-chlorophenyl)-6-ethylpyrimidin-1-ium 3-carboxybenzoate hydrate (1:1:1). *J. Mol. Struct.* 1224, 129309 (2021).
23. M.N. Tahir, M. Ashfaq, A.F. de la Torre, J. Caballero, E.W. Hernandez-Rodríguez, and A. Ali, Rationalizing the stability and interactions of 2,4-diamino-5-(4-chlorophenyl)-6-ethylpyrimidin-1-ium 2-hydroxy-3,5-dinitrobenzoate salt. *J. Mol. Struct.* 1193, 185–194 (2019).
24. S.M.A. Mashhadi, M.H. Bhatti, E. Jabeen, U. Yunus, M. Ashfaq, M. Akhtar, M.N. Tahir, S.M. Alshehri, and S.A. Ojha, Synthesis and antioxidant studies of 2,4-dioxothiazolidine-5-acetic acid based organic salts: SC-XRD and DFT approach. *ACS Omega* 8, 30186–30198 (2023).
25. M. Ashfaq, M.N. Tahir, A. Kuznetsov, S.H. Mirza, M. Khalid, and A. Ali, DFT and single crystal analysis of the pyrimethamine-based novel co-crystal salt: 2,4-diamino-5-(4-chlorophenyl)-6-ethylpyrimidin-1-ium:4-hydroxybenzoate:methanol:hydrate (1:1:1:1) (DEHMH). *J. Mol. Struct.* 1199, 127041 (2020).
26. S. Jamil, H.Y. Gondal, A. Ali, A. Hussain, N. Akram, M. Nisar, M.N. Tahir, M. Ashfaq, A.R. Raza, S. Muhammad, Z.M. Cheema, A. Mustafai, and M.Y. Sameeh, Benzimidazolium quaternary ammonium salts: synthesis, single crystal and Hirshfeld surface exploration supported by theoretical analysis. *R. Soc. Open Sci.* 11, 231094 (2023).
27. S.K. Wolff, D.J. Grimwood, J.J. McKinnon, M.J. Turner, D. Jayatilaka, M.A. Spackman, CRYSTAL EXPLORER, Version 3.1. University of Western Australia (2012).
28. S. Selvaraj, Computational study on the structural features, vibrational aspects, chemical shifts, and electronic properties of 1,4-dinitrosopiperazine-2-carboxylic acid: insights into donor–acceptor interactions and thermodynamic properties. *Int. Res. J. Multidiscip. Tech.* 6, 1–16 (2024).
29. R.M. Silverstein, and F.X. Webster, *Spectrometric Identification of Organic Compounds* (New York: Wiley, 2003).
30. A. Ram Kumar, S. Selvaraj, K.S. Jayaprakash, S. Gunasekaran, S. Kumaresan, J. Devanathan, K.A. Selvam, L. Ramadass, M. Mani, and P. Rajkumar, Multispectroscopic (FT-IR, FT-Raman, ^{1}H NMR and ^{13}C NMR) investigations on syringaldehyde. *J. Mol. Struct.* 1229, 129490 (2021).
31. V. Vijayalakshmi, N. Kanagathara, J. Janczak, M.K. Marchewka, M. Azam, and K. Senthilkumar, Structural, spectroscopic and second harmonic generation evaluation of 1,2,4-triazolinium tartrate–tartaric acid as a promising nonlinear optical material. *Opt. Mater.* 147, 114694 (2024).
32. L.I. Kozhevina, L.G. Skryabina, and Y.K. Tselinskii, The interpretation of the infrared spectrum of tartaric acid. *J. Appl. Spectrosc.* 33, 1347–1351 (1980).
33. S. Vidya, C. Ravikumar, I. Hubert Joe, P. Kumaradhas, B. Devipriya, and K. Raju, Vibrational spectra and structural studies of nonlinear optical crystal ammonium D, L-tartrate: a density functional theoretical approach. *J. Raman Spectrosc.* 42(4), 676–684 (2011).
34. A. Logeswari, N. Prabavathi, and M. Carry, Crystal growth, Hirshfeld surfaces and quantum chemical investigations of 3-amino-1,2,4-triazolinium hydrogen L-tartrate single crystal for nonlinear optical applications. *J. Mater. Sci. Mater. Electron.* 34, 359 (2023).
35. V.S. Joshi, and M.J. Joshi, FTIR spectroscopic and thermal studies of calcium tartrate trihydrate crystals grown by gel assistance. *Indian J. Phys.* 75A, 159–163 (2001).
36. E. Theodosoglou, A. Koroneos, T. Soldatos, T. Zorba, and K.M. Paraskevopoulos, Comparative Fourier Transform Infrared and

X-ray powder diffraction analysis of naturally occurring K-feldspars. *Bull. Geol. Soc. Greece* 43, 2752–2761 (2010).
37. H. Schmidbaur, A. Schier, and A. Bayler, The solution and solid-state structure of L-carnitine L-tartrate. *Z. Naturforsch. B* 53, 788–791 (1998).
38. N. Krishnan, and K. Sivaperuman, Crystal structure, Hirshfeld surface, physicochemical and nonlinear optical characteristics of (E)-4-(5-bromo-2-hydroxystyryl)-1-methyl pyridinium iodide (MBHPI) crystal. *J. Mater. Sci. Mater. Electron.* 35, 1189 (2024).
39. S.K. Nandhini, S. Sudhakar, S. Muniyappan, and P. Murugakoothan, Growth and characterization of a potential organic NLO single crystal: guanidinium 4-aminobenzene sulfonate (GuAS). *Mater. Today Proc.* 8, 256–263 (2019).
40. N. Kanagathara, N. Sivakumar, M.K. Marchewka, J. Janczak, A. Alsulmi, V. Yogaraj, and E. Murugan, Structure, spectroscopic, optical, photoluminescence, and thermal characterization of 2-amino 3-picolinium arsenate crystalline material. *J. Mater. Sci. Mater. Electron.* 34(21), 1573 (2023).
41. N. Sivakumar, and G. Anbalagan, Third-order optical nonlinear (Z-scan), birefringence, photoluminescence, mechanical and etching studies on melaminium levulinate monohydrate (MLM) single crystal for optical device applications. *Opt. Mater.* 60, 533–540 (2016).
42. R. Archana, S. Sudhahar, K. Sadayandi, M. Vidhya, S. Sagadevan, F. Mohammad, and J. Podder, Investigation of the optical, photoluminescence, and dielectric properties of p-toludinium picrate single crystals. *Chin. J. Phys.* 67, 283–292 (2020).
43. Y. Liu, M. Li, Q. Fang, Q. Lv, M. Wu, and S. Cao, Structural and photoluminescence properties of polyethylene glycol (PEG)-assisted growth co-doped ZnO nanorod arrays compared with pure ZnO nanorod arrays. *Chin. J. Phys.* 48, 523–531 (2010).
44. N. Sivakumar, S. Saha, N. Bandaru, and J.K. Rath, Development of $MAPbI_3{\cdot}H_2O$ and $MAPbI_3$ perovskite solar cells using TiO_2 and P3HT as charge transport layers. *J. Mater. Sci. Mater. Electron.* 35, 223 (2024).
45. N. Sivakumar, S. Saha, R. Madaka, N. Bandaru, and J.K. Rath, Investigation on the structural, spectral, and optical properties of $MAPbI_3{\cdot}H_2O$ and $MAPbI_3$ perovskite crystals for photovoltaic cells. *J. Mater. Sci. Mater. Electron.* 34, 1193 (2023).
46. G. Shanmugam, and S. Brahadeeswaran, Spectroscopic, thermal and mechanical studies on 4-methylanilinium p-toluenesulfonate—a new organic NLO single crystal. *Spectrochim. Acta A Mol. Biomol. Spectrosc.* 95, 177–183 (2012).
47. M.S. Silva, M. Cilense, E. Orhan, M.S. Goes, M.A.C. Machado, L.P.S. Santos, C.O.P. Santos, E. Longo, J.A. Varela, M.A. Zaghete, and P.S. Pizani, The nature of the photoluminescence in amorphized PZT. *J. Lumin.* 111, 205–213 (2005).
48. N. Kanagathara, F. MaryAnjalin, V. Ragavendran, D. Dhanasekaran, R. Usha, R.G.S. Rao, and M.K. Marchewka, Experimental and theoretical (DFT) investigation of crystallographic, spectroscopic and Hirshfeld surface analysis of anilinium arsenate. *J. Mol. Struct.* 1223, 128965 (2021).
49. G.R. Desiraju, T. Steiner, *The Weak Hydrogen Bond: In Structural Chemistry and Biology*. International Union of Crystallography Monographs on Crystallography, Oxford University Press (2001).
50. A. Ramalingam, S. Kansız, N. Dege, and S. Sambandam, Synthesis, crystal structure, DFT calculations and Hirshfeld surface analysis of 3-chloro-2,6-bis(4-chlorophenyl)-3-methylpiperidin-4-one. *J. Chem. Crystallogr.* 51, 273–287 (2020).
51. M.J. Turner, J.J. McKinnon, D. Jayatilaka, and M.A. Spackman, *CrystEngComm* 13, 1804–1813 (2011).
52. L. Houda, H. Amal, E.K. Badr, M. Ahmed, T.M. Joel, H.K. Tuncer, K.R. Youssef, and K.S. Nada, Crystal structure, Hirshfeld surface analysis, calculations of crystal voids, interaction energy and energy frameworks as well as density functional theory (DFT) calculations of 3-[2-(morpholin-4-yl)-ethyl]-5,5-diphenylimidazolidine-2,4-dione. *Acta Crystallogr. E* 80, 423–429 (2024).
53. C. Jelsch, K. Ejsmont, and L. Huder, The enrichment ratio of atomic contacts in crystals, an indicator derived from the Hirshfeld surface analysis. *IUCrJ* 1, 119–128 (2014).
54. S. Sankar, N. Kanagathara, V. Natarajan, and R.A.J. Cyril, Broadband dielectric spectroscopic investigation of melaminium bis(trichloroacetate) dihydrate—a nonlinear optical single crystal. *J. Mater. Sci. Mater. Electron.* 32, 10778–10788 (2021).
55. R. Ramalakshmi, S.S. Mary, S.S. Kirupavathy, S. Muthu, and R. Thomas, Growth, spectral, optical, electrical and computational analysis of sodium oxalate single crystals. *Heliyon* 7(3), e06527 (2021).
56. S.K. Balu, N.P. Shanker, M. Manikandan, N. Aparnadevi, T. Mukilraj, P. Manimuthu, and C. Venkateswaran, Crossover to negative dielectric constant in perovskite $PrMnO_3$. *Phys. Status Solidi (a)* 217(17), 2000230 (2020).
57. N.S. Kumar, M. Ganapathy, S. Sharmila, M. Shankar, M. Vimalan, and I.V. Potheher, ZnO/Ni (OH) 2 core-shell nanoparticles: synthesis, optical, electrical and photoacoustic property analysis. *J. Alloys Compd.* 703, 624–632 (2017).
58. C. Mo, L. Zhang, and G. Wang, Characteristics of dielectric behavior in nanostructured materials. *Nanostruct. Mater.* 6, 823–826 (1995).
59. S. Jayanthi, S. Shenbagavalli, M. Muthuvinayagam, and B. Sundaresan, Effect of nano TiO_2 on the transport, structural and thermal properties of PEMA–NaI solid polymer electrolytes for energy storage devices. *Mater. Sci. Eng. B* 285, 115942 (2022).
60. V. Gupta, K.K. Bamzai, P.N. Kotru, and B.M. Wanklyn, Dielectric properties, AC conductivity and thermal behaviour of flux grown cadmium titanate crystals. *Mater. Sci. Eng. B* 130, 163–172 (2008).
61. N. Goel, N. Sinha, and B. Kumar, Growth and properties of sodium tetraborate decahydrate single crystals. *Mater. Res. Bull.* 48, 1632–1636 (2013).
62. N. Sivakumar, N. Kanagathara, G. Bhagavannarayana, S. Kalainathan, and G. Anbalagan, Growth, crystalline perfection, optical, thermal, laser damage threshold and electrical characterization of melaminium levulinate monohydrate single crystal. *J. Cryst. Growth* 426, 86–94 (2015).
63. N. Kanagathara, S. Sankar, L. Saravanan, V. Natarajan, and S. Elangovan, Dielectric and Impedance Spectroscopic Investigation of (3-Nitrophenol)-2, 4, 6-Triamino-1, 3, 5-Triazine: an organic crystalline material. *Adv. Condens. Matter. Phys.* 2022(1), 6002025 (2022).
64. V. Parol, A.N. Prabhu, M.A. Taher, S.R.G. Naraharisetty, N.K. Lokanath, and V. Upadhyaya, A third-order nonlinear optical single crystal of 3,4-dimethoxy-substituted chalcone derivative with high laser damage threshold value: a potential material for optical power limiting. *J. Mater. Sci. Mater. Electron.* 31, 9133–9150 (2020).
65. N. Sivakumar, R. Jayavel, G. Anbalagan, and R.R. Yadav, Synthesis, growth, spectral, electrical, mechanical and thermal characterization of a potential optical material: γ-glycine single crystal. *Opt. Mater.* 80, 177–185 (2018).
66. S. Chopra, S. Sharma, T.C. Goel, and R.G. Mendiratta, Structural, dielectric and pyroelectric studies of $Pb_{1-x}Ca_xTiO_3$ thin films. *Solid State Commun.* 127, 299–304 (2003).
67. K. Prabakar, K. Narayandass, and D. Mangalaraj, Dielectric and electric modulus properties of vacuum evaporated $Cd_{0.8}Zn_{0.2}Te$ thin films. *Mater. Sci. Eng. B* 98, 225–231 (2003).
68. Y. Hosono, K. Harada, and Y. Yamashita, Crystal growth and electrical properties of lead-free piezoelectric material $(Na_{1/2}Bi_{1/2})TiO_3$–$BaTiO_3$. *Jpn. J. Appl. Phys.* 40, 5722–5726 (2001).
69. N.D. Pandya, J.H. Joshi, D.J. Dave, R.R. Hajiyani, H.O. Jethva, M.J. Joshi, and A.C. Parmar, Permittivity and conductivity studies

of Ni-doped Pb levo-tartrate crystals. *J. Mater. Sci. Mater. Electron.* 35, 1243 (2024).
70. S.A. Kalyan, S. Elangovan, R. Karthick, N. Kanagathara, M.K. Marchewka, and J. Janczak, Synthesis, XRD, spectral, photoluminescence, optical, electrical conductivity and dielectric studies on melamine–melaminium 2-acetyl benzoate dehydrate. *J. Mater. Sci. Mater. Electron.* 35, 2100 (2024).
71. C. Naveen, M. Muthuvinayagam, S. Vigneshwaran, and S.V. Arunachalam, Structural and electrical conductivity of aloe vera–PVA-based $Mg2^{+}$ ion-conducting biopolymer membranes for energy applications. *Mater. Sci. Eng. B* 321, 118477 (2025).
72. R. Vuilleumier, and D. Borgis, Hopping along hydrogen bonds. *Nat. Chem.* 4, 432–433 (2012).
73. M. Sayer, and M. Mansingh, Transport properties of semiconducting phosphate glasses. *Phys. Rev. B* 6, 4629–4643 (1972).
74. A. Graja, Production of the second harmonic of light in ammonium pentaborate and other powdered piezoelectric materials. *Phys. Status Solidi B* 27, K93–K97 (1968).
75. S.K. Kurtz, and T.T. Perry, A powder technique for the evaluation of nonlinear optical materials. *J. Appl. Phys.* 39, 3798–3813 (1968).